www.acsnano.org

Nonlinear Optical Responses of Janus MoSSe/ MoS₂ Heterobilayers Optimized by Stacking Order and Strain

Nguyen Tuan Hung,*^{,∇} Kunyan Zhang,[∇] Vuong Van Thanh, Yunfan Guo, Alexander A. Puretzky, David B. Geohegan, Jing Kong, Shengxi Huang,* and Riichiro Saito*



Downloaded via RICE UNIV on May 30, 2024 at 02:48:36 (UTC). See https://pubs.acs.org/sharingguidelines for options on how to legitimately share published articles.

Cite This: ACS Nano 2023, 17, 19877-19886



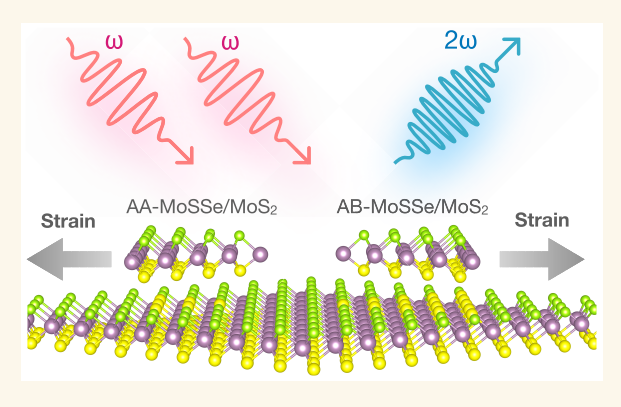
ACCESS I

III Metrics & More

Article Recommendations

Supporting Information

ABSTRACT: Nonlinear optical responses in second harmonic generation (SHG) of van der Waals heterobilayers, Janus MoSSe/MoS₂, are theoretically optimized as a function of strain and stacking order by adopting an exchange-correlation hybrid functional and a real-time approach in first-principles calculation. We find that the calculated nonlinear susceptibility, $\chi^{(2)}$, in AA stacking (550 pm/V) becomes three times as large as AB stacking (170 pm/V) due to the broken inversion symmetry in the AA stacking. The present theoretical prediction is compared with the observed SHG spectra of Janus MoSSe/MoS₂ heterobilayers, in which the peak SHG intensity of AA stacking becomes four times as large as AB stacking. Furthermore, a relatively large, two-dimensional strain (4%) that breaks the $C_{3\nu}$ point group symmetry of the MoSSe/MoS₂, enhances calculated $\chi^{(2)}$ values for both AA (900 pm/V) and AB (300 pm/V)



calculated $\chi^{(2)}$ values for both AA (900 pm/V) and AB (300 pm/V) stackings 1.6 times as large as that without strain.

KEYWORDS: second-harmonic generation, 2D Janus heterobilayers, stacking effect, strain engineering, first-principles calculations, time-dependent density-functional theory

1. INTRODUCTION

The van der Waals (vdW) heterobilayers such as MoS₂/WSe₂, ^{1,2} MoS₂/ZnO, ³ or graphene/h-BN⁴ have been extensively studied due to the functionalized interlayer coupling for electronic and optoelectronic properties. Recently, Zhang et al. ^{5,6} have successfully synthesized the Janus MoSSe/MoS₂ heterobilayers and reported the unconventional interlayer coupling between MoSSe and MoS₂ layers. Because of an intrinsic dipole moment in the Janus structures, we expect optical properties not only in the linear response but also in the nonlinear response. In this paper, we quantitatively investigate the nonlinear responses of MoSSe/MoS₂ heterobilayer by first-principles calculation as a function of stacking order and strain. The theoretical prediction is compared with a further experiment of the nonlinear optics for stacking order.

A Janus MoSSe layer has a sandwiched S–Mo–Se layer structure.⁷ Since the electronegativity of S and Se atoms are not the same, the Janus MoSSe has an intrinsic out-of-plane dipole moment, which enhances vdW interlayer coupling of the MoSSe/MoS₂ heterobilayers by 13.2% compared with MoS₂.⁵ Other van der Waals (vdW) heterobilayers of the Janus MXY (M = Mo, W; X/Y = S, Se, Te) and ZnO have been reported by

Idrees et al., ⁸ in which MoSSe/ZnO is a promising candidate for the photocatalytic water-splitting as a linear optical response based on the first-principles calculations. Since the Janus MoSSe has a broken mirror symmetry and an intrinsic out-of-plane dipole moment, their vdW heterobilayers are expected to show a better performance for electronic and optoelectronic devices than the conventional transition metal dichalcogenide (TMD). Since optical properties of the MoSSe/MoS₂ heterobilayers have been measured by the Raman and photoluminescence, ^{5,9} theoretical and experimental investigations of MoSSe/MoS₂ as a function of stacking order and strain may have optimized the nonlinear response.

Since the two-dimensional (2D) materials can accept much larger strains (up to 20%) compared with the bulk material, strain engineering is an efficient tool for tuning the electrical and

Received: May 17, 2023 Accepted: August 25, 2023 Published: August 29, 2023





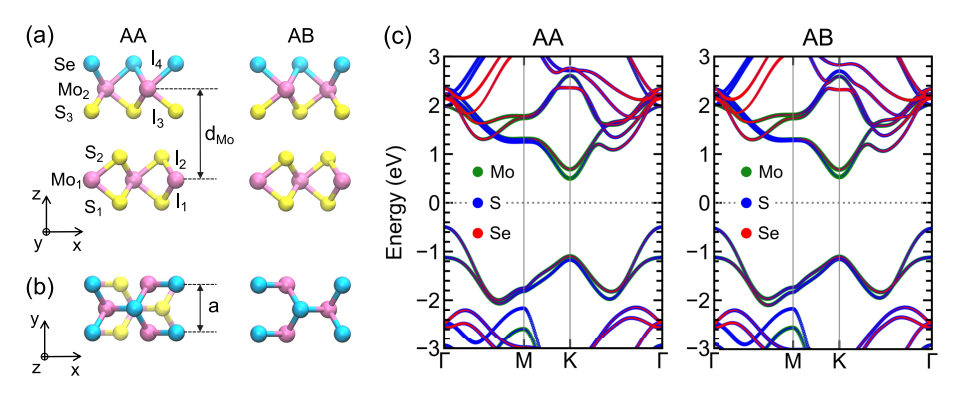


Figure 1. (a) Side and (b) top views of the optimized AA and AB stacking structures of MoSSe/MoS₂ heterobilayers, respectively. a, d_{Mo}, and l_{1,2,3,4} denote the lattice constant, the interlayer distance, and the bond lengths, respectively. x- and y-directions correspond to armchair and zigzag directions, respectively. (c) Electronic band structure of the AA- and AB-MoSSe/MoS₂ with atomic orbital projections in color.

optical properties of 2D materials as a flexible devices, 10,11 Lee et al. 12 reported that the strain of graphene is up to 25% with intrinsic stress $\sim 130 \pm 10$ GPa by using atomic force microscopy (AFM) nanoindentation. Theoretical calculations have also confirmed the large strains of graphene or TMDs based on density functional theory (DFT). 13,14 Strain engineering tells us several physical phenomena of graphene, such as the shifting of the Dirac point, 15 the superconductivity, 16 electroluminescence of circularly polarized light 17 and the redshift of the Raman mode. 11 For the 2D heterobilayers, Pak et al. 18 showed the strain-dependent interlayer coupling of MoS_2/WS_2 under the uniaxial strain, which allows the modulation of the electronic band structure for each monolayer. In this paper, we optimize the strains for the nonlinear susceptibility, $\chi^{(2)}$, of $MoSSe/MoS_2$.

Linear and nonlinear optical responses of the 2D vdW materials are sensitive to the symmetry of the lattice structure. 19,20 In finite numbers of 2H-MoS $_2$ layers, since the odd-number layers do not have spatial inversion symmetry, we observe second harmonic generation (SHG), while the evennumber layers that have inversion symmetry do not exhibit the SHG.²¹ For the 3R-MoS₂, SHG can be observed for both oddnumber and even-number layers since the AA stacking of the 3R-MoS₂ is intrinsically noncentrosymmetric.²² The noncentrosymmetric stacking is also obtained for the twisted MoS₂ bilayers, 23 dislocated WSe₂ nanoplates, 24 and spiral WS₂ nanosheets. 25,26 Boyd et al. 27 showed that the D_{3h} symmetry of the monolayer MoS2 has eight independent, nonzero SHG coefficients in the 6 \times 3 matrix of $\chi^{(2)}$ (see the Methods section for derivation). Wei et al.²⁸ showed that the Janus MoSSe monolayer with lower symmetry, C_{3v} , has 11 independent nonzero coefficients. Compared with MoS2, three additional nonzero coefficients associated with the z direction become nonzero due to the reduction of the symmetry. We expect that broken symmetry is an important factor in enhancing the SHG intensity. In this paper, we report the enhancement of $\chi^{(2)}$ as a function of laser excitation energy by strain engineering and selecting the stacking order of MoSSe/MoS₂. Two kinds of strain, biaxial and uniaxial strains, are investigated for possible AA and AB stackings structures in the calculation. We report that uniaxial strain breaks the in-plane symmetry of the 2D materials, leading to trade-off breaking of the nonlinear coefficients. Furthermore, we show that the biaxial strain leads to a significant decrease of the energy band gap due to the changing of the hopping parameters, 17 which are sensitive to the nonlinear response.

2. RESULTS AND DISCUSSION

2.1. Structure of Stacking and Electronic Structure. In Figure 1, we show the optimized structures of the AA- and AB-MoSSe/MoS₂ heterobilayers, respectively. The relaxed structure parameters are summarized in Table 1. The calculated lattice

Table 1. Lattice Constants (a), Interlayer Distance (d_{Mo}), and Bond Lengths ($l_{1,2,3,4}$) of AA- and AB-MoSSe/MoS₂

stacking	a (Å)	$d_{\mathrm{Mo}}\left(\mathring{\mathbf{A}}\right)$	l_1 (Å)	l_2 (Å)	l_3 (Å)	l ₄ (Å)
AA	3.33	6.26	2.48	2.48	2.47	2.59
AB	3.33	6.32	2.48	2.48	2.47	2.59

constant a and interlayer distance d_{Mo} are 3.33 Å (3.33 Å) and 6.26 Å (6.32 Å) for the AA (AB) stacking, whose values are close to the observed values (a=3.16 Å for the AA and AB stackings⁵). Since d_{Mo} of the AA stacking is smaller than that of AB stacking, the interlayer coupling of the AA stacking becomes stronger than that of AB stacking. Zhang et al.⁵ showed that the enhanced interlayer coupling is explained by the smaller interlayer spacing of polar Janus heterobilayers. We confirm it by showing that the intrinsic dipole moment of the AA stacking is larger than that of the AB stacking, as shown in Figure S3 in the Supporting Information. In order to discuss the stability of stacked Janus TMDs, we define the binding energies $E_{\rm b}(j)$, (j= AA or BB) of the heterobilayers as

$$E_{\rm b}(j) = E_{\rm stack}(j) - E_{\rm MoSSe} - E_{\rm MoS_2}$$
 (j = AA, AB) (1)

where $E_{\rm stack}(j)$, $E_{\rm MoSSe}(j)$, and $E_{\rm MoS_2}$ represent, respectively, the total energies of the stacked $(j={\rm AA, AB})$ MoSSe/MoS₂, the monolayer MoSSe, and the monolayer MoS₂. The calculated $E_{\rm b}({\rm AA}) = -0.164$ eV is slightly smaller than $E_{\rm b}({\rm AB}) = -0.162$ eV, which is consistent with the fact we find both the AA and AB structures in the experiment, as shown in Figure S1(a) in the Supporting Information. The Raman spectra in Figures S1(b) and (c) in the Supporting Information are used to confirm the stacking order in Figure S1(a).

It is important to note that the optimized lattice constants of the MoSSe and MoS₂ monolayers are 0.326 and 0.318 nm, respectively. Therefore, if there is no change of the lattice constants in the heterostructure, a lattice mismatch $\delta = 2.45\%$ between MoSSe and MoS₂ would produce a triangular moiré superlattice $\lambda = 0.326/\delta = 13.3$ nm for an angle-aligned MoSSe/MoS₂, which is larger than that of WSe₂/MoS₂ bilayers (~8.7

nm²⁹) and WSe₂/WS₂ bilayers (\sim 8 nm³⁰). Since the exciton radius (\sim 1–2 nm³¹) is larger than the lattice constants of MoSSe and MoS₂, and since the exciton radius is smaller than the moiré period of MoSSe/MoS₂, we can expect that the Moiré potential can trap an exciton, which leads to modifying the SHG intensity per area.³⁰ However, the vertical stacking of heterobilayers does not always give rise to a moiré superlattice. In fact, Hsu et al.³¹ showed that in the MoSe₂/WSe₂ heterobilayers grown by chemical vapor deposition methods, the minor lattice distortion in each layer leads to a commensurate atomic alignment without a moiré pattern. Since the observed PL spectra of MoSSe/MoS₂ do not have the moiré exciton peak, ^{5,6} the MoSSe/MoS₂ might not have the moiré pattern but the minor lattice distortion in each layer, which can be neglected to calculate the SHG.

In order to identify AA or AB by the Raman spectra in Figures S1(b) and S1(c) in the Supporting Information, we show the phonon dispersion of the AA- (solid line) and AB-MoSSe/MoS₂ (dotted line) in Figure S2 in the Supporting Information. The calculated phonon frequencies at the Γ point are consistent with the observed Raman spectra in Figures S1(b) and S1(c), in which the Raman spectra showed five peaks, that is, the out-ofplane A'_1 mode at 290 cm⁻¹ of the MoSSe layer, the in-plane E'mode at $382-384 \text{ cm}^{-1}$ and the A'_1 mode at $405-407 \text{ cm}^{-1}$ of the MoS₂ layer, and the interlayer shear and breathing modes at 22 and 38 cm⁻¹. The inset of Figure S2 shows that the shear mode of the AA stacking (17.46 cm⁻¹) appears at a higher frequency than that of AB stacking (13.89 cm⁻¹), which is consistent with the red-shift in the Raman experiment. The redshift in AB is originated by the larger interlayer interaction of AA stacking, where the interlayer force constant is proportional to the electric field.5

In Figure 1c, we show the electronic band structure with atomic orbital projections colored for the AA and AB-MoSSe/ MoS₂. The AA- and AB-MoSSe/MoS₂ show direct band gaps at the K point of 1.59 and 1.64 eV, respectively, which are calculated by using the HSE hybrid functional. Zhang et al.6 showed that Janus MoSSe/MoS2 has two photoluminescence (PL) peaks at 1.84 and 1.97 eV, both for AA- and AB-MoSSe/ MoS₂, which are close to the excitons of the monolayer MoS₂ at 1.85 and 2.00 eV.5 The calculated values of the indirect band gaps are close to the observed PL peak energy, although we do not consider the exciton effect. It is noted that the excitons of the monolayer MoSSe appear at 1.55 and 1.71 eV.5 This means that the two PL peaks of AA- and AB-MoSSe/MoS₂ mainly come from the constituent MoS₂ layer in the Janus bilayer. The contribution of each atom in the direct energy gap at the Γ point is S or Se atoms. On the other hand, the contribution of each atom in the direct energy gap at the K point is Mo atoms. Since we see, in Figure 1c, that the lowest conduction band at the Γ point has an S atom component, we expect that most of the photoexcited electrons gather in the MoS₂ in the heterobilayer, which might be a reason why we observed PL from MoS₂ in Janus MoSSe/MoS₂.

The SHG is favorable for the Janus bilayer, because of the intrinsic electric field between the MoSSe and MoS $_2$ layers. The electric field occurs in MoSSe/MoS $_2$ by the potential difference $\Delta\Phi$ between the MoSSe and MoS $_2$ layers. The calculated values of $\Delta\Phi$ are 0.833 and 0.625 eV for the AA- and AB-MoSSe/MoS $_2$, respectively, which means that AA-MoSSe/MoS $_2$ can give the larger SHG intensity. Even though Se atoms do not exist in the interlayer region, as shown in Figure 1a, we get the different values of $\Delta\Phi$ between AA and AB, whose reason is

explained by Figure S3 in the Supporting Information. In Figure S3, we show that the difference of $\Delta\Phi$ between AA and AB-MoSSe/MoS₂ occurs mainly at the interlayer region, which is sensitive to the stacking order. The difference in $\Delta\Phi$ between AA and AB comes from the fact that the relative positions of Se atoms to S atoms affect the Mo₁–S₂–S₃ chemical bonds in the interlayer region, as shown in Figures 1a and 1b. This situation is the microscopic reason why the SHG intensity is larger in AA than in AB.

2.2. Optical Responses and Stacking Effect. Let us discuss the optical responses of Janus TMDs. For a given electric field $\mathbf{E}(t)$, the induced polarization $\mathbf{P}(t)$ is expanded in power of \mathbf{E} as follows:²⁷

$$\mathbf{P}_{i}(t) = \epsilon_{0} \left(\chi_{ij}^{(1)} \mathbf{E}_{j}(t) + \chi_{ijk}^{(2)} \mathbf{E}_{j}(t) \mathbf{E}_{k}(t) + \dots \right)$$
(2)

where ϵ_0 is the vacuum permittivity, the subscripts i, j, and k in P and E refer to the Cartesian x,y,z components, $\chi^{(1)}$ is the linear susceptibility, and $\chi^{(2)}$ is the second-order nonlinear susceptibility. In the Yambo code, P(t) is calculated by the Berry-phase formulation of E(t). 32,33 The dielectric function can be directly calculated by $\chi^{(1)}$ as $\epsilon_{ii}(\omega) = 1 + 4\pi\chi_{ii}^{(1)}(\omega)$. 27

In Figure 2a, we show the real part ε_1 (dashed lines) and imaginary part ε_2 (solid lines) of the dielectric function, $\varepsilon = \varepsilon_1 +$

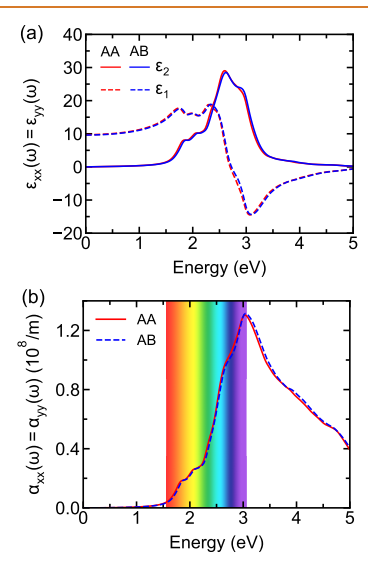


Figure 2. (a) Calculated real part ϵ_1 (dashed lines) and imaginary part ϵ_2 (solid lines) of the dielectric function, $\epsilon = \epsilon_1 + I\epsilon_2$, for the AA-and AB-MoSSe/MoS₂. (b) Calculated in-plane absorption coefficient $\alpha(\omega)$ as a function of energy $\hbar\omega$ for the AA (solid line) and AB stackings (dashed line). The color region represents the photon energy of the visible light region from 1.61 eV to 3.10 eV.

 $i\epsilon_2$, for the AA- and AB-stackings. Since the point groups of the Janus AA and AB-MoSSe/MoS $_2$ are C_{3w} we get the following relation: $\epsilon_{xx}(\omega) = \epsilon_{yy}(\omega)$. We can see that the difference in ϵ_1 or ϵ_2 between AA- and AB-MoSSe/MoS $_2$ can be negligible. Two peaks of ϵ_2 at 1.8 and 2.2 eV correspond to the optical transitions from the top of the valence bands to the bottom of the split conduction bands at the K point, while the peak at 2.6 eV corresponds to the optical transition at the Γ point. The calculated maximum values of ϵ_1 = 18.9 and ϵ_2 = 28.7 are comparable to the observed dielectric function of the 2H-MoTe $_2$ ($\epsilon_1 \sim 35$ and $\epsilon_2 \sim 27$ at 4.2 K) by using the spectroscopic ellipsometry. ³⁴

Breaking inversion symmetry in the Janus MoSSe/MoS₂ gives some nonzero matrix elements of second-order nonlinear optical susceptibility, $\chi_{ijk}^{(2)} \neq 0$ in eq 2 in which $\chi_{ijk}^{(2)}$ is given by a 6 × 3 matrix (see eq 14). In Figures 3a and 3b, we plot the

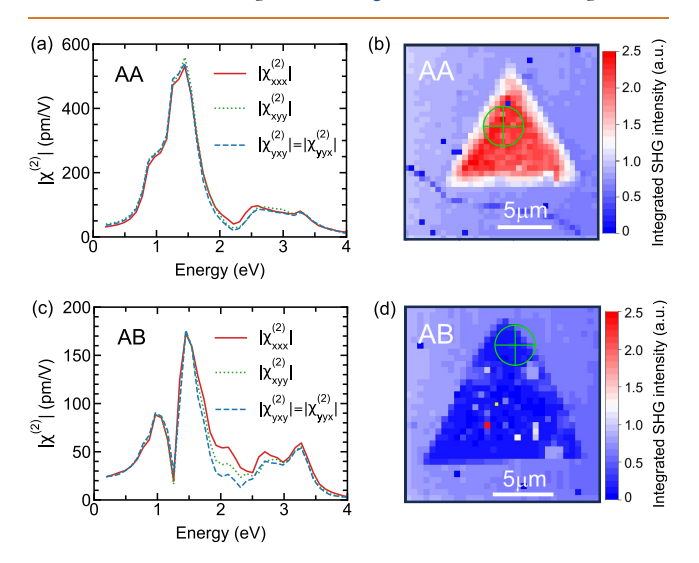


Figure 3. Absolute values of $\chi^{(2)}_{xxx}$ (solid line), $\chi^{(2)}_{xyy}$ (dashed line), and $\chi^{(2)}_{yxy} = \chi^{(2)}_{yyx}$ (dotted line) of the AA- (a) and AB-MoSSe/MoS₂ (c) as a function of photon energy. Integrated SHG intensity maps in arbitrary units of AA- (panel (b)) and AB-MoSSe/MoS₂ (panel (d)), respectively, in which the laser light at 828 nm was polarized along the armchair direction. The maps are measured with 0.5 μ m steps, and the SHG spectra are integrated from 380 nm to 450 nm. The corresponding SHG spectra at the locations marked by crosses on the maps are presented in Figure S1 in the Supporting Information.

absolute values of three nonzero components, $\chi_{xxxy}^{(2)}$, $\chi_{xyy}^{(2)}$, and $\chi_{yxy}^{(2)}$ of $\chi^{(2)}$ of AA- and AB-MoSSe/MoS₂ as a function of the photon energy, respectively. The calculated $\chi^{(2)}$ satisfies the relation between the elements of $\chi^{(2)}$ for the point group C_{3v} , $\chi_{xxx}^{(2)} = -\chi_{xyy}^{(2)} = -\chi_{yyx}^{(2)} = \chi_{yxx}^{(2)} = \chi_{xxy}^{(2)} = \chi_{xyx}^{(2)} = 0$, which is derived in the Methods section. It is noted that $\chi_{yxy}^{(2)} = \chi_{yyx}^{(2)}$ and $\chi_{xxy}^{(2)} = \chi_{xyx}^{(2)} = \chi_{xyx}^{$ due to the j and k are interchangeable in eq 2. Two peaks are found at ~1.0 and 1.5 eV, which are related to the intraband transitions from the two photons at the K and Γ points, respectively. The maximum value of $\chi^{(2)}$ of 173 pm/V of the AB stacking is consistent with that of the Janus MoSSe monolayer from the experiment (\sim 150–200 pm/V).³⁵ We note that our results are consistent with the previous works in which $\chi^{(2)}$ in the armchair direction, x, becomes nonzero. ^{27,28,35,36} By comparing Figures 3a and 3c, we understand that the maximum value of $\chi^{(2)}$ of 560 pm/V for AA-MoSSe/MoS₂ is 3.24 times larger than that of the AB-MoSSe/MoS₂. Moreover, we compare the $|\chi_{xxx}^{(2)}|$ of AA-MoSSe/MoS₂ with those of AA-MoSSe and AA-MoS₂ bilayers, as shown in Figure 4. We note that the AA and AB stackings correspond to the 3R and 2H phases of MoS2 or MoSSe. The calculated value of $|\chi_{xxx}^{(2)}|$ of AA-MoSSe/MoS₂ is comparable with those of AA-MoSSe and AA-MoS2 bilayers. This means that the stacking is more sensitive for optimizing the SHG of the heterostructure than the constituent layered materials. Hsu et al.²³ also observed that the SHG intensity of the heterostacked MoS₂, WSe₂/MoS₂, and WSe₂/WS₂ bilayers is not sensitive to the constituent layered materials.

To confirm the theoretical prediction, we have measured the integrated SHG intensity mapping of the AA- and AB-MoSSe/MoS₂ by a Ti-sapphire laser with a wavelength of 828 nm, as

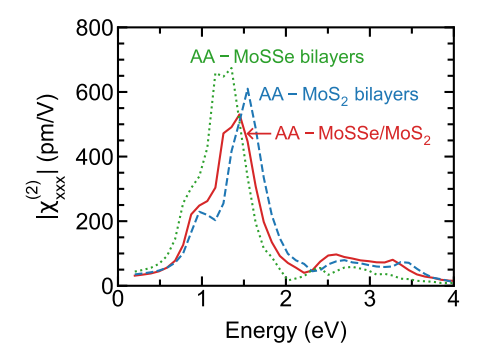


Figure 4. Absolute calculated values of $\chi^{(2)}_{xxx}$ as a function of photon energy for AA-MoSSe/MoS₂ heterobilayers, AA-MoSSe bilayers, and AA-MoS₂ bilayers.

shown in Figures 3b and 3d. The SHG spectra at the locations marked by crosses in Figures 3b and 3d are shown in Figure S4 in the Supporting Information, in which the maximum SHG intensity in arbitrary units of AA-MoSSe/MoS2 is ~1865 at 414 nm, which is ~ 3.93 times larger than that of AB-MoSSe/MoS₂ (475 at 414 nm). The 828 nm (or 1.497 eV) laser is selected for measuring SHG since the calculated SHG has the optimized peak at 1.5 eV, as shown in Figures 3a and 3c. The possible reason for the discrepancy of the intensity ratio at 1.5 eV between the experiment (3.93×) and theory (3.24×) might come from the dip of $\chi^{(2)}$ for AB-MoSSe/MoS₂ at ~1.25 eV. If the calculated result might shift to the higher energy, the expected value of $\chi^{(2)}$ for AB-MoSSe/MoS₂ could decrease significantly, compared with that for AA-MoSSe/MoS₂. This suggestion can be justified since we know that the exciton effect that we do not consider in the theoretical calculation pushes the excitation energy higher because of self-energy correction. The excitonic state gives a spatially localized wave function, which enhances the exciton-photon matrix element.³⁷ This leads to enhancement of the calculated dipole vector (d) and $\chi^{(2)}$ (see eq 6). This exciton effect might be the reason why we get different SHG intensity ratios of AA to AB stacking structures between theory and experiment. The SHG calculation, including the exciton effect for the MoSSe/MoS2 heterobilayer, should be a future work. We note that in Figures 3b and 3d, the triangle regions are the AA- and AB-MoSSe/MoS₂, respectively, and the surrounding region is the MoSSe monolayer. The average value of the SHG intensity of the MoSSe monolayer is about 700 ± 50 , which is larger than that of AA-MoSSe/MoS2 and smaller than that of AB-MoSSe/MoS₂. This order of the SHG is in agreement with the calculated result that $\chi^{(2)}$ at 1.55 eV of AB-MoSSe/ MoS_2 (155 pm/V) < MoSSe monolayer (211 pm/V) < AA-MoSSe/MoS₂ (423 pm/V). Based on this order of the SHG, we suggest that the SHG intensity can be used for distinguishing the Janus monolayer, AA, and AB Janus heterobilayers.

2.3. Strain Effect on Second Harmonic Generation. When we apply the Janus material as a flexible device, we need to evaluate the largest possible strain and strain-dependent energy gap and SHG intensity. In Figure 5a, we show the stress—strain curves of the AA- (solid line) and AB-MoSSe/MoS₂ (dotted line) for (1) biaxial strain s_{xy} , and (2) tensile strains (s_{xx}) along x-and (s_{yy}) y-directions, respectively. The fracture points are evaluated by the maximum value of stress, σ^{max} , and the corresponding strain, s^{max} , which are referred to as the ideal stress and the ideal strain for mechanical strength, respectively. ^{13,14,38} For the biaxial strain, the calculated values of (σ^{max}_{xy} ; s^{max}_{xy}) are (23.4 N/m, 0.21) and (23.1 N/m, 0.19) for the AA and

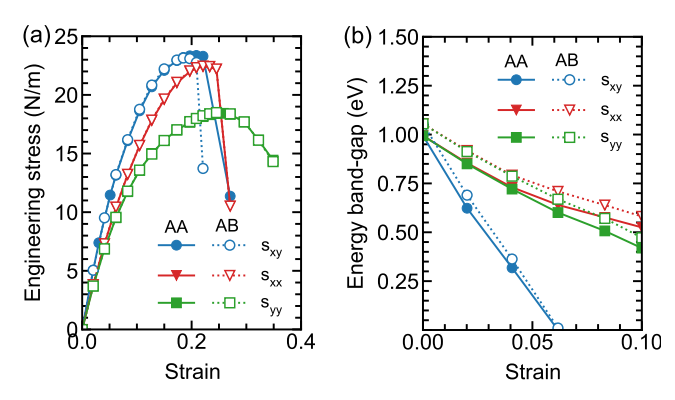


Figure 5. (a) Stress—strain curves of the AA- (solid line) and AB-MoSSe/MoS₂ (dotted line) for biaxial strain s_{xy} , and tensile strains (s_{xx}) along x- and (s_{yy}) y-directions, respectively. (b) Indirect band gap as a function of strain $(s_{xy}, s_{xx}, and s_{yy})$ for AA- (solid line) and AB-MoSSe/MoS₂ (dotted line).

AB stackings, respectively. For tensile strain, $(\sigma_{xx}^{max}; s_{xx}^{max})$ are (22.4 N/m, 0.22) and (22.5 N/m, 0.22) for the AA and AB stackings, respectively, and $(\sigma_{yy}^{max}; s_{yy}^{max})$ are (18.4 N/m, 0.26) and (18.5 N/m, 0.25) for the AA and AB stackings, respectively. The difference $(\sigma_{xy}^{max}; s_{xy}^{max})$ between the AA and AB stackings for each strain is negligible because the vdW interaction gives a small contribution to σ_{xy}^{max} compared with in-plane covalent bonding. In fact, the mechanical properties of the MoSSe/MoS₂ heterobilayers are almost the same as that of the MoS₂ 38 and MoSSe monolayers. The is important to point out that the ideal strain up to 0.19–0.26 (or 19% to 26%) is promising for the 2D flexibility device, in which strain engineering can tune the electronic properties of the material.

To demonstrate the flexibility of the Janus MoSSe/MoS₂ heterobilayers, we estimate in-plane Young's modulus (Y) and Poisson's ratio (ν), which are given by ^{39,40}

$$Y_{xx} = \frac{C_{11}C_{22} - C_{12}^2}{C_{22}}; \qquad Y_{yy} = \frac{C_{11}C_{22} - C_{12}^2}{C_{11}}$$
 (3)

and

$$\nu_{xy} = \frac{C_{12}}{C_{22}}; \qquad \nu_{yx} = \frac{C_{12}}{C_{11}}$$
(4)

where the elastic constants C_{ij} are given in Table S1 in the Supporting Information. The values of Y and ν are given in Table S1. Due to similar bonding types compared with the MoS₂ monolayer, Y and ν of 192–180 N/m and 0.27–0.28, respectively, of MoSSe/MoS₂ are similar to that of MoS₂ (Y = 180 \pm 60 N/m and ν = 0.14–0.2).

In Figure 5b, we show the indirect bandgap ($\Gamma \to K$) of the AA- (solid line) and AB-MoSSe/MoS₂ (dotted line), as a function of the strain. Here, the values of the band gap are corrected by the HSE calculations. For small strains, the variation of the energy band gap, ΔE_{gr} from the gap without strain is proportional to the strain as

$$\Delta E_{\rm g} \approx D_{\rm g}(s_{xx} + s_{yy}) \tag{5}$$

where we call $D_{\rm g}$ the band gap deformation potential. Using $s_{xx}=s_{yy}=s_{xy}$ (biaxial strain), $(s_{xx}\neq 0; s_{yy}=0)$ or $(s_{xx}=0; s_{yy}\neq 0)$ (tensile strain) to eq 5, the slope of $\Delta E_{\rm g}$ as a function of strain becomes double for the biaxial strain, compared with tensile strain, as shown in Figure 5b, in which semiconductor-metal transition occurs at $s_{xy}=0.06$ for the biaxial strain. By fitting the calculated data in Figure 5b to eq 5, we obtain the fitted values of $D_{\rm g}=8.15, 4.10$, and 5.43 eV for the biaxial strain and the tensile strains along x- and y-directions, respectively. It is noted that eq 5 might be suitable only for the case of strain s<0.1 and $E_{\rm g}>0$. In previous work, t0 we showed that, for strain t3 only the t3 value of the Janus TMDs shows nonlinear behavior to the strain.

In Figures 6a and 6b, we show the absolute values of the inplane $\chi^{(2)}$ as a function of the photon energy of AA- and AB-MoSSe/MoS₂ for several biaxial and tensile strains, respectively. Since the lattice deformation under the biaxial strain does not change the point group symmetry, $\chi^{(2)}_{xxx} = -\chi^{(2)}_{xyy} = -\chi^{(2)}_{yxy} = -\chi^{(2)}_{yyx}$ are found for both AA and AB-MoSSe/MoS₂, as shown in Figures 6a and 6d, respectively. On the other hand, since the $C_{3\nu}$

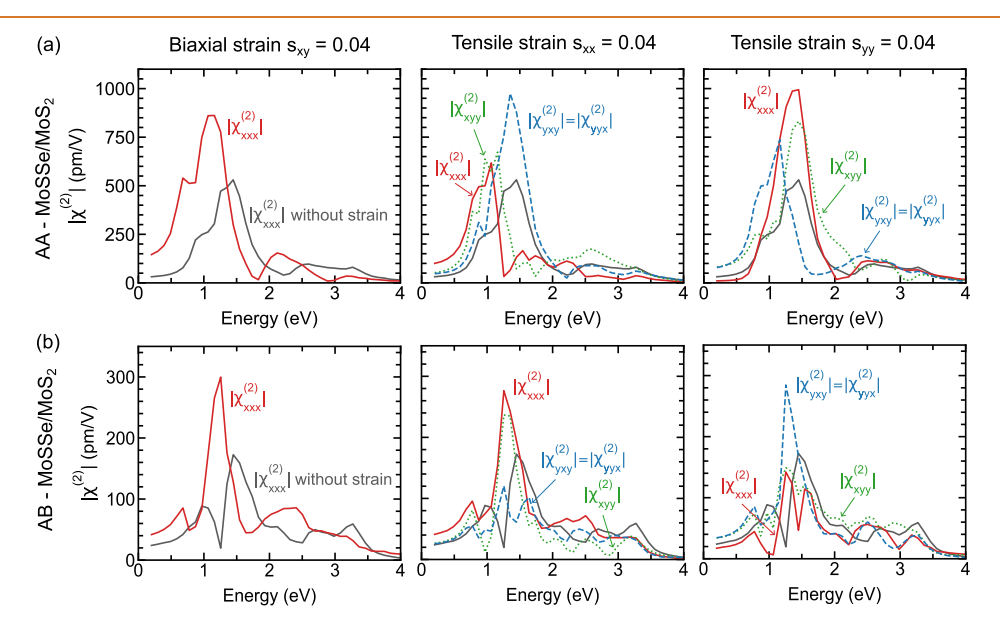


Figure 6. (a) Absolute values of $\chi^{(2)}$ ($\chi^{(2)}_{xxxy}$, $\chi^{(2)}_{xyy}$ and $\chi^{(2)}_{yxy} = \chi^{(2)}_{yyx}$) of AA-MoSSe/MoS₂ as a function of photon energy for biaxial strain $s_{xy} = 0.04$, and tensile strains along x- ($s_{xx} = 0.04$) and y-directions ($s_{yy} = 0.04$), respectively. (b) $|\chi^{(2)}|$ of AB-MoSSe/MoS₂ as a function of photon energy for s_{xy} , s_{xxy} and s_{yy} respectively. $\chi^{(2)}_{xxy}$ without strain (black line) is plotted as the reference value.

symmetry is broken for the tensile strains, three independent inplane susceptibilities appear: $\chi^{(2)}_{xxxy}$, $\chi^{(2)}_{xyy}$ and $\chi^{(2)}_{yxy} = \chi^{(2)}_{yyx}$, as shown in Figures 6a and 6b. Furthermore, since $E_{\rm g}$ decreases with increasing strain s, $\chi^{(2)}$ increases as a function of s. It is noted that we know $E_{\rm g}$ -dependent SHG, which is derived for the Si(111) surface (with C_{3y} , symmetry) by 43,44

$$\chi^{(2)} = \frac{3e}{E_{\rm g}} \chi^{(1)} \mathbf{d} \tag{6}$$

where **d** is the dipole matrix elements. The calculated results show that $\chi^{(2)}$ can be enhanced almost twice for both biaxial and tensile strains, s=0.04, compared without strain s=0. The calculated results are consistent with the experimental strain-induced SHG for the MoS₂⁴⁵ and MoSe₂ monolayers, ⁴⁶ in which the tensile strain is applied by using a two-point bending technique and get some enhancement of $\chi^{(2)}$ about 49% relative change per 0.01 strain. Thus, we ask for an experiment of AA-MoSSe/MoS₂ with a strain of 0.04 for observing large $\chi^{(2)}$ values close to 1000 pm/V.

3. CONCLUSION

In summary, we have presented stacking-order-dependent and strain-dependent nonlinear optical properties of Janus MoSSe/MoS₂ heterobilayers. Our results show that the lack of inversion symmetry of the Janus MoSSe/MoS₂ leads to the nonzero of the nonlinear susceptibility components, $\chi^{(2)}_{xxxx} = -\chi^{(2)}_{xyy} = -\chi^{(2)}_{yxy} \neq 0$. The nonlinear susceptibilities $\chi^{(2)}$ of MoSSe/MoS₂ can be controlled by stacking and strain engineering due to breaking of the mirror and in-plane symmetries, respectively. $\chi^{(2)}$ of the AA-MoSSe/MoS₂ is three times larger than that of the AB-MoSSe/MoS₂. Thus, we suggest that the SHG intensity can be used as an efficient method to distinguish between the AA and AB Janus heterobilayers instead of Raman spectra. On the other hand, MoSSe/MoS₂ heterobilayer exhibits good mechanical properties with the ideal strain up to ~20%, making MoSSe/MoS₂ as a flexible material for the optoelectronic and nonlinear optical applications, such as the bulk photovoltaic or four-wave mixing.

4. METHODS

4.1. First-Principles Calculations. We perform all DFT calculations with Quantum ESPRESSO, 47 which uses a plane-wave basis set to describe the wave function of electrons.⁴⁸ We adopt the optimized norm-conserving Vanderbilt pseudopotentials⁴⁹ with the Perdew-Burke-Ernzerhof (PBE) exchange-correlation functional. St Kinetic energy cutoff is set to 85 Ry, and k-point meshes are set to $12 \times$ 12×1 and $24 \times 24 \times 1$ for the self-consistent and nonself-consistent calculations, respectively. It is noted that the kinetic energy cutoff and kpoint meshes are selected based on the well-converged electronic structures and optical properties. The spin-orbit coupling (SOC) is not included in the optical calculations to save computation time since including SOC does not affect the second-order nonlinear spectra of Janus MoSSe.³⁶ To obtain accurate band gaps, the Heyd-Scuseria-Ernzerhof (HSE) hybrid functional based on PBE⁵¹ and Wannier90 package⁵² are used to calculate and interpolate the energy band dispersion. The phonon dispersion is obtained by using the density functional perturbation theory (DFPT)⁵³ calculations, in which **q**-point mesh is set to $8 \times 8 \times 1$. The Coulomb cutoff for the 2D system is adopted to remove the long-range interactions in the vacuum direction, which is important to obtain the correct phonon dispersion in 2D materials.

In order to construct the supercell of the $MoS_2/MoSSe$ heterobilayers, the out-of-plane lattice parameter is fixed with a sufficient vacuum spacing of ~ 17 Å. To accurately describe the vdW interaction between the MoS_2 and MoSSe layers, we adopt the nonlocal functional vdW-DF2^{SS} for all calculations. The lattice parameters and

the atomic positions are optimized by using the BFGS quasi-newton algorithm, in which the convergence is determined when the interatomic forces and all stress components are less than 0.00001 Ry/a.u. and 0.01 GPa, respectively. All structures are also optimized for each step of strain.

The linear and nonlinear optical responses are calculated by real-time time-dependent DFT calculations as implemented in the Yambo code. ⁵⁶ The real-time approach is based on the equation of motion for the valence state derived by the real-time Schrödingder equation: ³²

$$i\hbar \frac{\mathrm{d}}{\mathrm{d}t} |v_{\mathbf{k}m}\rangle = (\mathcal{H}_{\mathbf{k}}^0 + \Delta \mathcal{H}_{\mathbf{k}} + \mathcal{E} \cdot \partial_{\mathbf{k}}) |v_{\mathbf{k}m}\rangle$$
 (7)

where m is the valence band index and $\nu_{\rm k\; m}$ is the time-dependent valence state at the wave vector k. $\mathcal{H}^0_{\mathbf{k}}$ is the unperturbed Kohn-Sham Hamiltonian, which is obtained by Quantum ESPRESSO. $\Delta \mathcal{H}_k$ is the uniform scissor shift, which can be obtained by the HSE functional or GW approximation. ³² The final term $\mathcal{E} \cdot \partial_{\mathbf{k}}$ corresponds to the coupling between the valence state and external electric field \mathcal{E} . The timedependent polarization of the system is calculated with these valence band states. The equation of motion is integrated with a 0.01 fs time step for a total simulation time of 55 fs with a damping factor of 0.15 eV. The number of G-vectors participating in the equation of motion is 50 000. We multiply the calculated values by the ratio of the out-ofplane lattice parameter to the thickness of the MoS₂/MoSSe heterobilayers (1.3 nm). We note that Attaccalite et al. reported that the SHG intensity with the Bethe-Salpeter equation that includes the exciton effect is closer to the independent particle approximation (IPA) (without exciton effect) for the monolayer GaSe and InSe. Therefore, in the present study, SHG is performed by IPA with a uniform scissor shift correction, which is determined by the HSE functional, to optimize the computation time.

4.2. Sample Fabrication. MoSSe/MoS₂ heterostructures with AA and AB stackings were synthesized through the direct selenization of bilayer MoS₂ grown by chemical vapor deposition. During the selenization process, bilayer MoS₂ on SiO₂/Si substrates was placed in a quartz tube in a furnace with selenium powder placed upstream of the quartz tube. The base pressure was first pumped to 10 mTorr to remove the residual air. Then, the hydrogen plasma with a power of 50 W and H₂ flow of 20 sccm was introduced to the quartz tube to strip off the top-layer sulfur atoms and replace the top sulfur layer with selenium. The selenization substitutes the top atomic layer, while preserving the stacking order at the interface. Therefore, the synthesized MoSSe/MoS₂ possess the same AA and AB stacking as their parent MoS₂ bilayers.

4.3. Optical Spectroscopy. The second harmonic generation of MoSSe/MoS₂ was measured using a 40 fs Ti:sapphire laser at 800 nm with 80 MHz repetition rate. The fundamental laser beam was passed through a half-wave plate and focused onto a sample surface using a 100× microscope objective (NA = 0.9) to a \sim 1 μ m spot. The power density on the sample was $\sim 0.2 \text{ mW}/\mu\text{m}^2$. The SHG light was collected in a backscattering configuration where the SHG was passed through a short-pass filter with a cutoff at 650 nm to filter out the fundamental excitation light at 828 nm and a polarization filter to select the SHG polarization parallel to that of the excitation light. The SHG signal was finally collected by a monochromator coupled to a microscope and equipped with a 150 grooves/mm grating and a CCD camera (Pixis 256BR, Princeton Instruments). Raman measurements were performed using a Horiba Labram spectrometer using a 532 nm excitation with a 100× objective. The Raman spectrometer utilized an 1800/mm grating, providing a spectral accuracy of 0.1 cm⁻¹.

4.4. Second-Order Susceptibility Analysis of 2D Janus Heterobilayers. Here we derive a relationship between elements of the second-order susceptibility tensor $\chi^{(2)}$ for $C_{3\nu}$ point group symmetry. From eq 2, the nonlinear polarization is given by 27

$$\mathbf{P}^{(2)} = \epsilon_0 \chi^{(2)} \mathbf{E}^2 \tag{8}$$

We note that if inversion is symmetric, which implies ${\bf P} \to -{\bf P}$ and ${\bf E} \to -{\bf E}$, $\chi^{(2)}$ must be zero. Thus, the lack of inversion symmetry of the Janus structure is needed to obtain nonzero values of $\chi^{(2)}$.

Next, we rotate $P^{(2)}$ by an angle θ about the z-axis as follows:

$$R\mathbf{P}^{(2)} = \epsilon_0 R\chi^{(2)} [R]^{-1} R\mathbf{E}^2 \tag{9}$$

where R is the rotation matrix around the z-axis, which is given by

$$R = \begin{pmatrix} R_{xx} & R_{xy} & 0 \\ R_{yx} & R_{yy} & 0 \\ 0 & 0 & 1 \end{pmatrix} = \begin{pmatrix} \cos \theta & -\sin \theta & 0 \\ \sin \theta & \cos \theta & 0 \\ 0 & 0 & 1 \end{pmatrix}$$
(10)

and

$$R^{(2)} = \begin{pmatrix} R_{xx}R_{xx} & R_{xy}R_{xy} & 0 & 0 & 0 & R_{xx}R_{xy} \\ R_{yx}R_{yx} & R_{yy}R_{yy} & 0 & 0 & 0 & R_{yx}R_{yy} \\ 0 & 0 & 1 & 0 & 0 & 0 \\ 0 & 0 & 1 & R_{yy} & R_{yx} & 0 \\ 0 & 0 & 1 & R_{xy} & R_{xx} & 0 \\ R_{xx}R_{yx} & R_{xy}R_{yy} & 0 & 0 & 0 & R_{xx}R_{yy} \end{pmatrix}$$

$$\tag{11}$$

From eq 9, the rotated electric filed \mathbf{E}' is given by

$$\mathbf{E}'^{2} \equiv R^{(2)}\mathbf{E}^{2} = \begin{pmatrix} E'_{x}E'_{x} \\ E'_{y}E'_{y} \\ E'_{z}E'_{z} \\ 2E'_{y}E'_{z} \\ 2E'_{x}E'_{z} \\ 2E'_{x}E'_{y} \end{pmatrix}$$
(12)

where

$$E'_{x} = R_{xx}E_{x} + R_{xy}E_{y}$$

$$E'_{y} = R_{yx}E_{x} + R_{yy}E_{y}$$

$$E'_{z} = E_{z}$$
(13)

and rotated $\chi^{(2)}$ is given by

$$\chi'^{(2)} \equiv R\chi^{(2)}[R]^{-1} = \begin{pmatrix} \chi_{xxx'}^{(2)} & \chi_{xyy'}^{(2)} & \chi_{xzz'}^{(2)} & \chi_{xyz'}^{(2)} & \chi_{xxy'}^{(2)} \\ \chi_{yxx'}^{(2)} & \chi_{yyy'}^{(2)} & \chi_{yzz'}^{(2)} & \chi_{yyz'}^{(2)} & \chi_{yxz'}^{(2)} & \chi_{yxy'}^{(2)} \\ \chi_{zxx'}^{(2)} & \chi_{zyy'}^{(2)} & \chi_{zzz'}^{(2)} & \chi_{zyz'}^{(2)} & \chi_{zxz'}^{(2)} & \chi_{zxy'}^{(2)} \end{pmatrix}$$

$$(14)$$

In the case of the $C_{3\nu}$ symmetry of the MoSSe/MoS₂ heterobilayer, we get the following equations that $\chi^{(2)}$ is invariant for $\theta = 120^{\circ}$. Here, θ is defined by the angle between the electric field $\mathbf{E}(\omega)$ and the x-direction (armchair). By inserting $\theta = 120^{\circ}$ into eq 10, and from eq 14, we have

$$\chi_{xxx'}^{(2)} = -\frac{1}{2}(\chi_{xxx}^{(2)} + \sqrt{3}\chi_{xxy}^{(2)} + \sqrt{3}\chi_{yxx}^{(2)} + 3\chi_{yxy}^{(2)})$$

$$\chi_{xyy'}^{(2)} = \frac{1}{2}(\sqrt{3}\chi_{xxx}^{(2)} - \chi_{xyy}^{(2)} + 3\chi_{yxy}^{(2)} - \sqrt{3}\chi_{yyy}^{(2)})$$

$$\chi_{xxy'}^{(2)} = \frac{1}{2}(\sqrt{3}\chi_{xxx}^{(2)} + 2\chi_{xxy}^{(2)} - \sqrt{3}\chi_{xyy}^{(2)} + 3\chi_{yxx}^{(2)} + 2\sqrt{3}\chi_{yxy}^{(2)} - 3\chi_{yyy}^{(2)})$$

$$\chi_{xxx'}^{(2)} = \frac{1}{4}(\chi_{xxx}^{(2)} + \sqrt{3}\chi_{xyx}^{(2)} + 3\chi_{yxx}^{(2)} + \sqrt{3}\chi_{yyz}^{(2)})$$

$$\chi_{xxx'}^{(2)} = -\frac{1}{4}(\sqrt{3}\chi_{xxx}^{(2)} - \chi_{xyz}^{(2)} + 3\chi_{yxx}^{(2)} - \sqrt{3}\chi_{yyz}^{(2)})$$

$$\chi_{xxx'}^{(2)} = -\frac{1}{2}(\chi_{xxx}^{(2)} + \sqrt{3}\chi_{xyy}^{(2)} + \chi_{xyy}^{(2)} + \chi_{yyy}^{(2)})$$

$$\chi_{yyy'}^{(2)} = -\frac{1}{2}(3\chi_{xxx}^{(2)} + 3\chi_{xxy}^{(2)} - \chi_{yxx}^{(2)} + \chi_{yyy}^{(2)})$$

$$\chi_{yxx'}^{(2)} = -\frac{1}{2}(3\chi_{xxx}^{(2)} + 2\sqrt{3}\chi_{xyy}^{(2)} + 3\chi_{xyy}^{(2)} - \sqrt{3}\chi_{yxy}^{(2)})$$

$$\chi_{yxx'}^{(2)} = -\frac{1}{4}(\sqrt{3}\chi_{xxx}^{(2)} + 3\chi_{xyz}^{(2)} - \chi_{yxx}^{(2)} - \chi_{yxy}^{(2)} - \chi_$$

Next, we select only the in-plane $\chi^{(2)}$ from eq 15, in which $\chi^{(2)} = {\chi'}^{(2)}$ by rotation $\theta = 120^{\circ}$, we have

$$\chi_{xxxx}^{(2)} = \chi_{xxxx'}^{(2)} = -\frac{1}{2}(\chi_{xxx}^{(2)} + \sqrt{3}\chi_{xxy}^{(2)} + \sqrt{3}\chi_{yxx}^{(2)} + 3\chi_{yxy}^{(2)})$$

$$\chi_{xyy}^{(2)} = \chi_{xyy'}^{(2)} = \frac{1}{2}(\sqrt{3}\chi_{xxy}^{(2)} - \chi_{xyy}^{(2)} + 3\chi_{yxy}^{(2)} - \sqrt{3}\chi_{yyy}^{(2)})$$

$$\chi_{xxxy}^{(2)} = \chi_{xxy'}^{(2)}$$

$$= \frac{1}{2}(\sqrt{3}\chi_{xxx}^{(2)} + 2\chi_{xxy}^{(2)} - \sqrt{3}\chi_{xyy}^{(2)} + 3\chi_{yxx}^{(2)} + 2\sqrt{3}\chi_{yxy}^{(2)} - 3\chi_{yyy}^{(2)})$$

$$\chi_{yyy}^{(2)} = \chi_{yyy'}^{(2)} = -\frac{1}{2}(3\chi_{xxx}^{(2)} - \sqrt{3}\chi_{xxy}^{(2)} + \sqrt{3}\chi_{yxy}^{(2)} + \chi_{yyy}^{(2)})$$

$$\chi_{yxx}^{(2)} = \chi_{yxx'}^{(2)} = \frac{1}{2}(\sqrt{3}\chi_{xxx}^{(2)} + 3\chi_{xxy}^{(2)} - \chi_{yxx}^{(2)} + \sqrt{3}\chi_{yxy}^{(2)})$$

$$\chi_{yxy}^{(2)} = \chi_{yxy'}^{(2)}$$

$$= -\frac{1}{2}(3\chi_{xxx}^{(2)} + 2\sqrt{3}\chi_{xxy}^{(2)} + 3\chi_{xyy}^{(2)} - \sqrt{3}\chi_{yxx}^{(2)} - 2\chi_{yxy}^{(2)} - \sqrt{3}\chi_{yyy}^{(2)})$$

$$(16)$$

By solving eq 16, we obtain

$$\chi_{xxx}^{(2)} = -\chi_{xyy}^{(2)} = -\chi_{yxy}^{(2)} \qquad \chi_{yyy}^{(2)} = \chi_{yxx}^{(2)} = \chi_{xxy}^{(2)} = 0$$
 (17)

ASSOCIATED CONTENT

Supporting Information

The Supporting Information is available free of charge at https://pubs.acs.org/doi/10.1021/acsnano.3c04436.

Optical image of AA- and AB-MoSSe/MoS₂ and the Raman spectra, phonon dispersion of AA- and AB-MoSSe/MoS₂, electrostatic potential along the z-direction of the AA- and AB-MoSSe/MoS₂, table of the elastic constants, Young's modulus and Poisson's ratio, SHG spectra, and calculated SHG of AA-MoS₂ and AA-MoSSe bilayers (PDF)

AUTHOR INFORMATION

Corresponding Authors

Nguyen Tuan Hung — Frontier Research Institute for Interdisciplinary Sciences, Tohoku University, Sendai 980-8578, Japan; Department of Physics, Tohoku University, Sendai 980-8578, Japan; orcid.org/0000-0003-4156-6230; Email: nguyen.tuan.hung.e4@tohoku.ac.jp

Shengxi Huang — Department of Electrical and Computer Engineering, Rice University, Houston, Texas 77005, United States; orcid.org/0000-0002-3618-9074; Email: shengxi.huang@rice.edu

Riichiro Saito — Department of Physics, Tohoku University, Sendai 980-8578, Japan; Email: r.saito.sendai@gmail.com

Authors

Kunyan Zhang — Department of Electrical and Computer Engineering, Rice University, Houston, Texas 77005, United States; ⊕ orcid.org/0000-0002-6830-409X

Vuong Van Thanh – School of Mechanical Engineering, Hanoi University of Science and Technology, Hanoi 100000, Viet Nam; orcid.org/0000-0001-5243-0254

Yunfan Guo – Department of Chemistry, Zhejiang University, Hangzhou, Zhejiang 310058, China

Alexander A. Puretzky — Center for Nanophase Materials Sciences, Oak Ridge National Laboratory, Oak Ridge, Tennessee 37831, United States; orcid.org/0000-0002-9996-4429

David B. Geohegan – Center for Nanophase Materials Sciences, Oak Ridge National Laboratory, Oak Ridge, Tennessee 37831, United States

Jing Kong — Department of Electrical Engineering and Computer Science, Massachusetts Institute of Technology, Cambridge, Massachusetts 02139, United States; orcid.org/0000-0003-0551-1208

Complete contact information is available at: https://pubs.acs.org/10.1021/acsnano.3c04436

Author Contributions

 ${}^
abla ext{These authors contributed equally to this work.}$

Notes

The authors declare no competing financial interest.

ACKNOWLEDGMENTS

N.T.H. acknowledges financial support from the Frontier Research Institute for Interdisciplinary Sciences, Tohoku University. R.S. acknowledges JSPS Kakenhi No. JP22H00283. K.Z. and S.H. acknowledge National Science Foundation (Grant Nos. ECCS-2246564 and ECCS-1943895). S.H. also acknowledges funding from the Air Force Office of Scientific Research (AFOSR) under Grant No. FA9550-22-1-

0408. Y.G. and J.K. acknowledge the financial support from U.S. Department of Energy (DOE), Office of Science, Basic Energy Sciences under Award No. DE-SC0020042. The SHG measurements were supported by the Center for Nanophase Materials Sciences (CNMS), which is a U.S. Department of Energy, Office of Science User Facility at Oak Ridge National Laboratory.

REFERENCES

- (1) Kim, J.; Jin, C.; Chen, B.; Cai, H.; Zhao, T.; Lee, P.; Kahn, S.; Watanabe, K.; Taniguchi, T.; Tongay, S.; Crommie, M. F.; Wang, F. Observation of Ultralong Valley Lifetime in WSe₂/MoS₂ Heterostructures. *Sci. Adv.* **2017**, *3*, No. e1700518.
- (2) Vikraman, D.; Hussain, S.; Truong, L.; Karuppasamy, K.; Kim, H.-J.; Maiyalagan, T.; Chun, S.-H.; Jung, J.; Kim, H.-S. Fabrication of MoS₂/WSe₂ Heterostructures as Electrocatalyst for Enhanced Hydrogen Evolution Reaction. *Appl. Sur. Sci.* **2019**, *480*, 611–620.
- (3) Wang, S.; Ren, C.; Tian, H.; Yu, J.; Sun, M. MoS₂/ZnO van der Waals Heterostructure as A High-Efficiency Water Splitting Photocatalyst: A First-Principles Study. *Phys. Chem. Chem. Phys.* **2018**, 20, 13394–13399.
- (4) Leven, I.; Maaravi, T.; Azuri, I.; Kronik, L.; Hod, O. Interlayer Potential for Graphene/h-BN Heterostructures. *J. Chem. Theory Comput.* **2016**, 12, 2896–2905.
- (5) Zhang, K.; Guo, Y.; Ji, Q.; Lu, A.-Y.; Su, C.; Wang, H.; Puretzky, A. A.; Geohegan, D. B.; Qian, X.; Fang, S.; Kaxiras, E.; Kong, J.; Huang, S. Enhancement of van der Waals Interlayer Coupling Through Polar Janus MoSSe. *J. Am. Chem. Soc.* **2020**, *142*, 17499–17507.
- (6) Zhang, K.; Guo, Y.; Larson, D. T.; Zhu, Z.; Fang, S.; Kaxiras, E.; Kong, J.; Huang, S. Spectroscopic Signatures of Interlayer Coupling in Janus MoSSe/MoS₂ Heterostructures. *ACS Nano* **2021**, *15*, 14394–14403.
- (7) Thanh, V. V.; Van, N. D.; Truong, D. V.; Saito, R.; Hung, N. T. First-principles Study of Mechanical, Electronic and Optical Properties of Janus Structure in Transition Metal Dichalcogenides. *Appl. Surf. Sci.* **2020**, *526*, No. 146730.
- (8) Idrees, M.; Din, H.; Rehman, S. U.; Shafiq, M.; Saeed, Y.; Bui, H.; Nguyen, C. V.; Amin, B. Electronic Properties and Enhanced Photocatalytic Performance of van der Waals Heterostructures of ZnO and Janus Transition Metal Dichalcogenides. *Phys. Chem. Chem. Phys.* **2020**, *22*, 10351–10359.
- (9) Trivedi, D. B.; Turgut, G.; Qin, Y.; Sayyad, M. Y.; Hajra, D.; Howell, M.; Liu, L.; Yang, S.; Patoary, N. H.; Li, H.; Petric, M. M.; Meyer, M.; Kremser, M.; Barbone, M.; Soavi, G.; Stier, A. V.; Muller, K.; Yang, S.; Esqueda, I. S.; Zhuang, H.; Finley, J. J.; Tongay, S. Room-Temperature Synthesis of 2D Janus Crystals and their Heterostructures. *Adv. Mater.* **2020**, 32, No. 2006320.
- (10) Conley, H. J.; Wang, B.; Ziegler, J. I.; Haglund, R. F., Jr; Pantelides, S. T.; Bolotin, K. I. Bandgap Engineering of Strained Monolayer and Bilayer MoS₂. *Nano Lett.* **2013**, *13*, 3626–3630.
- (11) Yoon, D.; Son, Y. W.; Cheong, H. Strain-Dependent Splitting of The Double-Resonance Raman Scattering Band in Graphene. *Phys. Rev. Lett.* **2011**, *106*, No. 155502.
- (12) Lee, C.; Wei, X.; Kysar, J. W.; Hone, J. Measurement of The Elastic Properties and Intrinsic Strength of Monolayer Graphene. *Science* **2008**, 321, 385–388.
- (13) Liu, F.; Ming, P.; Li, J. Ab initio Calculation of Ideal Strength and Phonon Instability of Graphene under Tension. *Phys. Rev. B* **2007**, *76*, No. 064120.
- (14) Tuan Hung, N.; Van Truong, D.; Van Thanh, V.; Saito, R. Intrinsic Strength and Failure Behaviors of Ultra-Small Single-Walled Carbon Nanotubes. *Comput. Mater. Sci.* **2016**, *114*, 167–171.
- (15) Pereira, V. M.; Castro Neto, A. H.; Peres, N. M. R. Tight-Binding Approach to Uniaxial Strain in Graphene. *Phys. Rev. B* **2009**, *80*, No. 045401.
- (16) Si, C.; Liu, Z.; Duan, W.; Liu, F. First-principles Calculations on The Effect of Doping and Biaxial Tensile Strain on Electron-Phonon Coupling in Graphene. *Phys. Rev. Lett.* **2013**, *111*, No. 196802.

- (17) Wang, S.; Ukhtary, M. S.; Saito, R. Strain Effect on Circularly Polarized Electroluminescence in Transition Metal Dichalcogenides. *Phys. Rev. Res.* **2020**, *2*, No. 033340.
- (18) Pak, S.; Lee, J.; Lee, Y.-W.; Jang, A.-R.; Ahn, S.; Ma, K. Y.; Cho, Y.; Hong, J.; Lee, S.; Jeong, H. Y.; Im, H.; Shin, H. S.; Morris, S. M.; Cha, S. N.; Sohn, J. I.; Kim, J. M. Strain-Mediated Interlayer Coupling Effects on The Excitonic Behaviors in An Epitaxially Grown MoS₂/WS₂ van der Waals Heterobilayer. *Nano Lett.* **2017**, *17*, 5634–5640.
- (19) Wang, J.; Mi, Y.; Gao, X.; Li, J.; Li, J.; Lan, S.; Fang, C.; Shen, H.; Wen, X.; Chen, R.; Liu, X.; He, T.; Li, D. Giant Nonlinear Optical Response in 2D Perovskite Heterostructures. *Adv. Opt. Mater.* **2019**, *7*, No. 1900398.
- (20) Autere, A.; Jussila, H.; Dai, Y.; Wang, Y.; Lipsanen, H.; Sun, Z. Nonlinear Optics with 2D Layered Materials. *Adv. Mater.* **2018**, *30*, No. 1705963.
- (21) Shi, J.; et al. 3R MoS₂ with Broken Inversion Symmetry: A Promising Ultrathin Nonlinear Optical Device. *Adv. Mater.* **2017**, *29*, No. 1701486.
- (22) Rajarapu, R.; Barman, P. K.; Yadav, R.; Biswas, R.; Devaraj, M.; Poudyal, S.; Biswal, B.; Laxmi, V.; Pradhan, G. K.; Raghunathan, V.; Nayak, P. K.; Misra, A. Pulsed Carrier Gas Assisted High-Quality Synthetic 3 R-Phase Sword-like MoS₂: A Versatile Optoelectronic Material. *ACS Nano* **2022**, *16*, 21366–21376.
- (23) Hsu, W.-T.; Zhao, Z.-A.; Li, L.-J.; Chen, C.-H.; Chiu, M.-H.; Chang, P.-S.; Chou, Y.-C.; Chang, W.-H. Second Harmonic Generation from Artificially Stacked Transition Metal Dichalcogenide Twisted Bilayers. ACS Nano 2014, 8, 2951–2958.
- (24) Shearer, M. J.; Samad, L.; Zhang, Y.; Zhao, Y.; Puretzky, A.; Eliceiri, K. W.; Wright, J. C.; Hamers, R. J.; Jin, S. Complex and Noncentrosymmetric Stacking of Layered Metal Dichalcogenide Materials Created by Screw Dislocations. *J. Am. Chem. Soc.* **2017**, 139, 3496–3504.
- (25) Ci, P.; Zhao, Y.; Sun, M.; Rho, Y.; Chen, Y.; Grigoropoulos, C. P.; Jin, S.; Li, X.; Wu, J. Breaking Rotational Symmetry in Supertwisted WS₂ Spirals via Moiré Magnification of Intrinsic Heterostrain. *Nano Lett.* **2022**, 22, 9027–9035.
- (26) Fan, X.; Jiang, Y.; Zhuang, X.; Liu, H.; Xu, T.; Zheng, W.; Fan, P.; Li, H.; Wu, X.; Zhu, X.; Zhang, Q.; Zhou, H.; Hu, W.; Wang, X.; Sun, L.; Duan, X.; Pan, A. Broken Symmetry Induced Strong Nonlinear Optical Effects in Spiral WS₂ Nanosheets. *ACS Nano* **2017**, *11*, 4892–4898.
- (27) Boyd, R. W. Nonlinear Optics; Academic Press: Cambridge, MA, 2020.
- (28) Wei, Y.; Xu, X.; Wang, S.; Li, W.; Jiang, Y. Second Harmonic Generation in Janus MoSSe A Monolayer and Stacked Bulk with Vertical Asymmetry. *Phys. Chem. Chem. Phys.* **2019**, *21*, 21022–21029.
- (29) Zhang, C.; Chuu, C.-P.; Ren, X.; Li, M.-Y.; Li, L.-J.; Jin, C.; Chou, M.-Y.; Shih, C.-K. Interlayer Couplings, Moiré Patterns, and 2D Electronic Superlattices in MoS₂/WSe₂ Hetero-Bilayers. *Sci. Adv.* **2017**, 3, e1601459.
- (30) Jin, C.; Regan, E. C.; Yan, A.; Iqbal Bakti Utama, M.; Wang, D.; Zhao, S.; Qin, Y.; Yang, S.; Zheng, Z.; Shi, S.; Watanabe, K.; Taniguchi, T.; Tongay, S.; Zettl, A.; Wang, F. Observation of Moiré Excitons in WSe₂/WS₂ Heterostructure Superlattices. *Nature* **2019**, *567*, 76–80.
- (31) Hsu, W.-T.; Lu, L.-S.; Wu, P.-H.; Lee, M.-H.; Chen, P.-J.; Wu, P.-Y.; Chou, Y.-C.; Jeng, H.-T.; Li, L.-J.; Chu, M.-W.; Chang, W. H. Negative Circular Polarization Emissions from WSe₂/MoSe₂ Commensurate Heterobilayers. *Nat. Commun.* **2018**, *9*, 1356.
- (32) Attaccalite, C.; Grüning, M. Nonlinear Optics from An Ab initio Approach by Means of The Dynamical Berry Phase: Application to Second-and Third-Harmonic Generation in Semiconductors. *Phys. Rev. B* **2013**, *88*, No. 235113.
- (33) Souza, I.; Íniguez, J.; Vanderbilt, D. Dynamics of Berry-Phase Polarization in Time-Dependent Electric Fields. *Phys. Rev. B* **2004**, *69*, No. 085106.
- (34) Gulo, D. P.; Hung, N. T.; Sankar, R.; Saito, R.; Liu, H.-L. Exploring Optical Properties of 2H- and 1T'- MoTe₂ Single Crystals by Spectroscopic Ellipsometry. *Phys. Rev. Mater.* **2023**, *7*, No. 044001.
- (35) Petric, M. M.; Villafane, V.; Herrmann, P.; Ben Mhenni, A.; Qin, Y.; Sayyad, Y.; Shen, Y.; Tongay, S.; Muller, K.; Soavi, G.; Finley, J. J.;

- Barbone, M. Nonlinear Dispersion Relation and Out-of-Plane Second Harmonic Generation in MoSSe and WSSe Janus Monolayers. *Adv. Optical Mater.* **2023**, No. 2300958.
- (36) Strasser, A.; Wang, H.; Qian, X. Nonlinear Optical and Photocurrent Responses in Janus MoSSe Monolayer and MoS₂-MoSSe van der Waals Heterostructure. *Nano Lett.* **2022**, 22, 4145–4152.
- (37) Jiang, J.; Saito, R.; Sato, K.; Park, J.; Samsonidze, G. G.; Jorio, A.; Dresselhaus, G.; Dresselhaus, M. Exciton-Photon, Exciton-Phonon Matrix Elements, and Resonant Raman Intensity of Single-Wall Carbon Nanotubes. *Phys. Rev. B* **2007**, *75*, No. 035405.
- (38) Li, T. Ídeal Strength and Phonon Instability in Single-Layer MoS₂. *Phys. Rev. B* **2012**, *85*, No. 235407.
- (39) Hung, N. T; Nugraha, A. R T; Saito, R. Two-Dimensional MoS₂ Electromechanical Actuators. *J. Phys. D: Appl. Phys.* **2018**, *51*, No. 075306.
- (40) Thanh, V. V.; Van, N. D.; Truong, D. V.; Hung, N. T. Charge-Induced High-Performance Actuation of Borophene. *J. Phys. D: Appl. Phys.* **2021**, *54*, No. 105504.
- (41) Casillas, G.; Santiago, U.; Barron, H.; Alducin, D.; Ponce, A.; Jose-Yacaman, M. Elasticity of MoS₂ Sheets by Mechanical Deformation Observed by In Situ Electron Microscopy. *J. Phys. Chem. C* **2015**, *119*, 710–715.
- (42) Peelaers, H.; Van de Walle, C. G. Effects of Strain on Band Structure and Effective Masses in MoS₂. *Phys. Rev. B* **2012**, *86*, No. 241401.
- (43) Jha, S. S.; Bloembergen, N. Nonlinear Optical Susceptibilities in Group-IV and III-V Semiconductors. *Phys. Rev.* **1968**, *171*, 891.
- (44) Phillips, J. C.; Van Vechten, J. Nonlinear Optical Susceptibilities of Covalent Crystals. *Phys. Rev.* **1969**, *183*, 709.
- (45) Mennel, L.; Furchi, M. M.; Wachter, S.; Paur, M.; Polyushkin, D. K.; Mueller, T. Optical Imaging of Strain in Two-Dimensional Crystals. *Nat. Commun.* **2018**, *9*, 516.
- (46) Liang, J.; Zhang, J.; Li, Z.; Hong, H.; Wang, J.; Zhang, Z.; Zhou, X.; Qiao, R.; Xu, J.; Gao, P.; Liu, Z.; Liu, Z.; Sun, Z.; Meng, S.; Liu, K.; Yu, D. Monitoring Local Strain Vector in Atomic-Layered MoSe₂ by Second-Harmonic Generation. *Nano Lett.* **2017**, *17*, 7539–7543.
- (47) Giannozzi, P.; Baroni, S.; Bonini, N.; Calandra, M.; Car, R.; Cavazzoni, C.; Ceresoli, D.; Chiarotti, G. L.; Cococcioni, M.; Dabo, I.; Dal Corso, A.; de Gironcoli, S.; Fabris, S.; Fratesi, G.; Gebauer, R.; Gerstmann, U.; Gougoussis, C.; Kokalj, A.; Lazzeri, M.; Martin-Samos, L.; Marzari, N.; Mauri, F.; Mazzarello, R.; Paolini, S.; Pasquarello, A.; Paulatto, L.; Sbraccia, C.; Scandolo, S.; Sclauzero, G.; Seitsonen, A. P.; Smogunov, A.; Umari, P.; Wentzcovitch, R. M. QUANTUM ESPRESSO: A Modular and Open-Source Software Project for Quantum Simulations of Materials. *J. Phys.: Condens. Matter* 2009, 21, No. 395502.
- (48) Hung, N. T.; Nugraha, A. R. T.; Saito, R. Quantum ESPRESSO Course for Solid-State Physics; Jenny Stanford Publishing: New York, 2022.
- (49) Hamann, D. Optimized Norm-Conserving Vanderbilt Pseudopotentials. *Phys. Rev. B* **2013**, *88*, No. 085117.
- (50) Perdew, J. P.; Burke, K.; Ernzerhof, M. Generalized Gradient Approximation Made Simple. *Phys. Rev. Lett.* **1996**, *77*, 3865.
- (51) Heyd, J.; Scuseria, G. E.; Ernzerhof, M. Hybrid Functionals Based on A Screened Coulomb Potential. *J. Chem. Phys.* **2003**, *118*, 8207–8215.
- (52) Mostofi, A. A.; Yates, J. R.; Lee, Y. S.; Souza, I.; Vanderbilt, D.; Marzari, N. Wannier90: A Tool for Obtaining Maximally-Localised Wannier Functions. *Comput. Phys. Commun.* **2008**, *178*, 685–699.
- (53) Baroni, S.; de Gironcoli, S.; Dal Corso, A.; Giannozzi, P. Phonons and Related Crystal Properties from Density-Functional Perturbation Theory. *Rev. Mod. Phys.* **2001**, *73*, 515–562.
- (54) Sohier, T.; Calandra, M.; Mauri, F. Density Functional Perturbation Theory for Gated Two-Dimensional Heterostructures: Theoretical Developments and Application to Flexural Phonons in Graphene. *Phys. Rev. B* **2017**, *96*, No. 075448.

- (55) Lee, K.; Murray, É. D.; Kong, L.; Lundqvist, B. I.; Langreth, D. C. Higher-Accuracy van der Waals Density Functional. *Phys. Rev. B* **2010**, 82, No. 081101.
- (56) Marini, A.; Hogan, C.; Grüning, M.; Varsano, D. Yambo: An Ab initio Tool for Excited State Calculations. *Comput. Phys. Commun.* **2009**, *180*, 1392–1403.